

Titan's middle-atmospheric temperatures and dynamics observed by the Cassini Composite Infrared Spectrometer

Richard K. Achterberg^{a,*}, Barney J. Conrath^b, Peter J. Gierasch^b, F. Michael Flasar^c,
Conor A. Nixon^a

^a University of Maryland, Department of Astronomy, College Park, MD 20742, USA

^b Department of Astronomy, Cornell University, Ithaca, NY 14853, USA

^c NASA Goddard Space Flight Center, Greenbelt, MD 20771, USA

Received 31 May 2007; revised 13 September 2007

Available online 10 January 2008

Abstract

The Composite Infrared Radiometer–Spectrometer (CIRS) instrument, on the NASA Cassini Saturn orbiter, has been acquiring thermal emission spectra from the atmosphere of Titan since orbit insertion in 2004. Observation sequences for measuring stratospheric temperatures have been obtained using both a nadir mapping mode and a limb viewing mode. The limb observations give better vertical resolution, and give information from higher altitudes, while the nadir observations provide more complete longitude coverage. Because the scale height of Titan's atmosphere is large enough so that emission from a grazing ray is influenced by horizontal temperature variations in the atmosphere, we have developed a two-dimensional temperature retrieval algorithm for reducing the limb spectra, which solves simultaneously for meridional and vertical temperature variations. The analyzed nadir mapping data have sampled nearly all longitudes at latitudes from about 90° S to 60° N, providing temperatures between pressure levels of about 5 to 0.2 mbar. The limb data covers latitudes between about 75° S and 85° N, and yields temperatures between about 1 and 0.005 mbar, at a small number of longitudes. The retrieved temperatures are consistent with early results from nadir observations [Flasar, F.M., and 44 colleagues, 2005. *Science* 308, 975–978] between 0.5 and 5 mbar where both results are valid, with the warmest temperatures at the equator, and much stronger meridional temperature gradients in the northern (winter) hemisphere than in the southern. At higher altitudes not probed by nadir viewing, the limb data reveal that the stratopause is nearly 20 K warmer in the northern polar regions than at the equator and southern hemisphere, and that the altitude of the stratopause shifts from ≈ 0.1 mbar (300 km) near the equator to 0.01 mbar (400 km) poleward of about 40° N. When the gradient wind equation is used to construct a zonal mean wind, the reversal in sign of the temperature leads to capping of the winter westerly flow. The core of the resulting jet is about 190 m s^{-1} in magnitude, spans between 30° N and 60° N, and peaks near 0.1 mbar. Estimates of the radiative heating associated with the radiative disequilibrium lead to a meridional overturning timescale of about three Earth years. © 2007 Elsevier Inc. All rights reserved.

Keywords: Titan; Atmospheres, structure; Atmospheres, dynamics; Infrared observations

1. Introduction

The earliest temperature determinations for Titan's stratosphere were made by the Voyager 1 infrared spectrometer (IRIS) (Flasar et al., 1981). The latitude variation of temperature from about 50° S latitude to about 60° N, at pressure levels between about 0.4 and 1.0 mbar in Titan's stratosphere was determined in November 1980, just after Titan's northern spring

equinox (February 1980). The latitudinal temperature gradient was found to be too large to be dynamically supported unless centrifugal acceleration balanced the latitudinal pressure gradient, leading to the conclusion that Titan's atmosphere, like that of Venus, exhibits rapid spin. Here we report new temperature determinations inferred from mid infrared spectra obtained by the NASA Cassini orbiter Composite Infrared Spectrometer (CIRS). The spectra were obtained between July 2004 and September 2006, after the northern hemisphere winter solstice on Titan (October 2002). Observations were made both of the limb, to collect information from high elevations, and in a nadir

* Corresponding author. Fax: +1 301 286 0212.

E-mail address: richard.k.achterberg@nasa.gov (R.K. Achterberg).

mapping mode, to give good spatial coverage at deeper levels. Altogether, the coverage reported here permits construction of a height, latitude cross-section from about 75° S to 75° N and between pressure levels approximately from 0.01 to 5 mbar, a range of over six pressure scale heights in the upper stratosphere and lower mesosphere. In addition, the maps may be used to study longitudinal structure, such as propagating waves. This report is a follow-up to a preliminary presentation of early mapping results (Flasar et al., 2005). At that time there were no limb observations and, as a result, the height coverage was more restricted.

Other techniques have been used to observe the structure and dynamics of Titan's atmosphere. Kostiuk et al. (2005) review wind determinations made by Doppler heterodyne spectroscopy, and report on recent measurements made immediately prior to the arrival of Cassini at Saturn. This type of measurement is particularly valuable because it gives an unambiguous determination of the sign of stratospheric zonal winds, which cannot be obtained from temperature measurements or stellar occultations (to be discussed below). The first successful measurements were in 1993 (Fast et al., 1994). From that time through to the present (Kostiuk et al., 2005), Doppler spectroscopy has consistently shown that Titan's stratospheric rotation is in the same direction as that of the satellite itself, which is locked in a 1:1 spin-orbit resonance with one side facing Saturn (Lemmon et al., 1993).

Central flash events in stellar occultations give information about the spin of Titan's upper stratosphere by revealing an oblate shape to density surfaces, which cannot be in static equilibrium with the satellite's gravitational field (see, e.g., Hubbard et al., 1993). This technique applies at altitudes where pressures are on the order of 0.2 to 0.8 mbar, but it has relatively poor horizontal resolution, restricted by the number of observing sites. Titan's winds at these levels are expected to vary seasonally: the radiative relaxation time in the upper stratosphere is relatively short (Flasar et al., 1981; Flasar and Conrath, 1990), implying that temperatures vary seasonally, and the zonal winds and zonal mean temperatures are coupled through the thermal wind equation, as discussed in Section 3. Wind profiles or partial profiles exist for July 1989 (Hubbard et al., 1993; Sicardy et al., 1999), December 2001 (Bouché, 2003), and November 2003 (Sicardy et al., 2006). Fig. 1 indicates the seasonal times when wind determinations have been made, and Fig. 2 displays a comparison of wind profiles from these four sets of data. The seasonal trends are complicated, but there is a suggestion that wind velocities are highest in the winter hemisphere.

Doppler shift of the radio signals from the Huygens Probe gave direct *in situ* determination of the vertical profile of zonal wind at about 10° S latitude, between the surface (1.5 bar) and 140 km altitude (~ 3 mbar pressure) (Bird et al., 2005; Folkner et al., 2006). At altitudes above 8 km, the measurements show that the winds are westerly (in the same direction as Titan's rotation) and increase with altitude. However, above 65 km there is a region of strong negative shear, and the winds decrease and nearly vanish at 75 km. At higher levels, they increase strongly with altitude, reaching $\sim 60 \text{ m s}^{-1}$ by 100 km altitude (10 mbar). This is approximately the base of

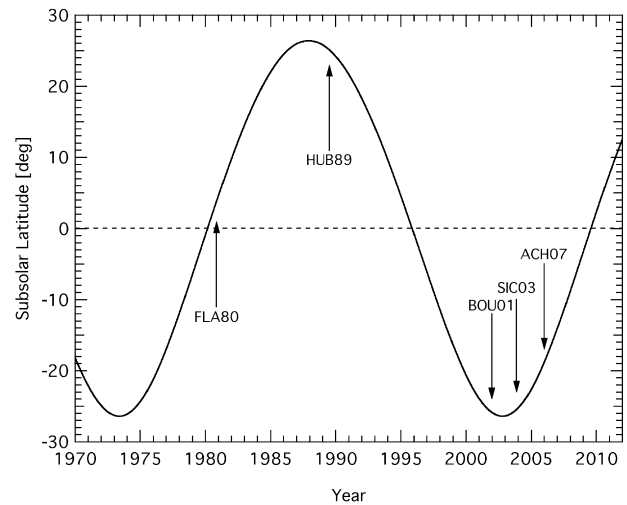


Fig. 1. Season and time for previous wind determinations. The year of the observation is indicated at the tail of the arrow, along with the first author's shortened name. FLA80 (Flasar et al., 1981) and ACH06 (the present work) are based on thermal winds from infrared spectrometers on Voyager and Cassini. HUB89 (Hubbard et al., 1993), BOU01 (Bouché, 2003) and SIC03 (Sicardy et al., 2006) are from stellar occultation campaigns.

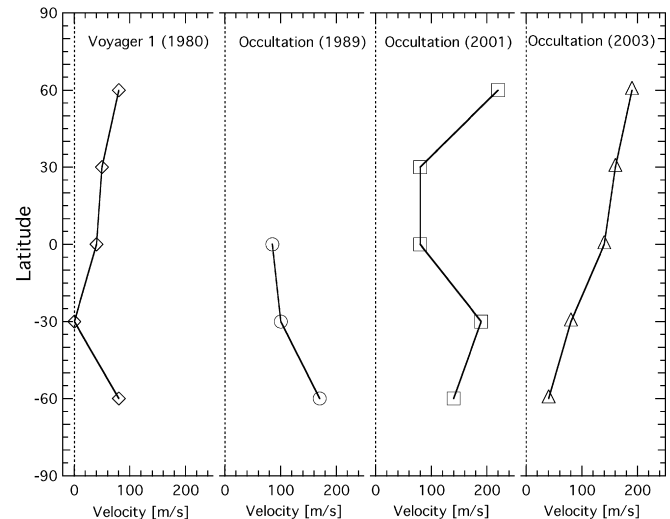


Fig. 2. Schematic indication of Voyager 1 thermal wind estimates (Flasar et al., 1981) and stellar occultation wind determinations from occultations in 1989 (Hubbard et al., 1993), 2001 (Bouché, 2003) and 2003 (Sicardy et al., 2006). Points are plotted only every 30° for easy comparison of the global patterns. The 1989 wind profile of Hubbard et al. (1993) is plotted only in the southern hemisphere where information exists (Bouché, 2003).

the stratospheric region where our temperature determinations exist, and we shall refer back to these results in Section 3, where we will need a boundary condition for a thermal wind integration.

Other seasonal changes, less directly connected to temperature observations, are observed on Titan. At the time of the Voyager encounters (L_S close to zero, northern spring equinox) the southern hemisphere appeared brightest at visible wavelengths. Lorenz et al. (1997) showed that the asymmetry was one point on a complicated seasonal cycle involving the global mean albedo as well as a latitudinal asymmetry. Furthermore,

the hemispheric brightness difference reverses sign between the blue and the near infrared. These changes in Titan's haze properties may be related to chemical transports caused by the general circulation and its seasonal changes. Hourdin et al. (2004) have studied the behavior of a Titan climatological model with parameterized eddy transports, and find that with appropriate parameter choices, the seasonal variations of hazes and hydrocarbons seem consistent with observations. The seasonal cycle on Titan is particularly complicated, in large part because the radiative and chemical time constants for adjustment to equilibrium vary with height. Furthermore, coupling with dynamics introduces major uncertainties because neither modeling nor observations have yet identified the dominant dynamical heat transport modes, not to mention their seasonal variations (Flasar and Conrath, 1990; Tokano et al., 1999). The temperature determinations reported here will provide a much more detailed and stringent test for models.

Because of the geometric thickness of Titan's atmosphere, interpretation of the spectra taken in limb viewing mode must take into account horizontal temperature variations in the atmosphere. The largest of these are due to latitudinal temperature gradients. In Section 2 a two-dimensional temperature retrieval algorithm is developed for inversion of limb spectra. In addition, a correction procedure is introduced for the one-dimensional inversion of spectra taken on the disk but at an angle, in the presence of horizontal temperature gradients. In Section 3 zonal mean results are presented and discussed, including display of thermal winds consistent with the temperature field. In Section 4, the implications for the mean meridional circulation of Titan's stratosphere are discussed.

2. Data and retrievals

2.1. Data

The stratospheric thermal structure analyzed in this investigation was retrieved from spectra acquired with Focal Plane 4 (FP4) of the CIRS instrument in the 1100 to 1400 cm^{-1} spectral region with a selectable apodized spectral resolution between 0.5 and 15.5 cm^{-1} . Each pixel of the 10-element linear array has a field of view of 0.28 mrad. The instrument and its calibration are described in detail by Flasar et al. (2004).

Both nadir-viewing and limb-viewing measurements are used. The nadir data were acquired using mapping sequences taken typically within a range of 250,000 to 400,000 km, giving a spatial resolution of 1.5° to 2.5° of great circle arc. Using a series of continuous slews of the instrument, each map covers essentially the entire Titan disk visible from the spacecraft. Fourteen maps with 2.8 cm^{-1} spectral resolution were completed during the time period included in this study; collectively, they provide quasi-global coverage. Five limb-viewing maps were also obtained at a typical spacecraft range of 120,000 km, yielding a geometric vertical resolution on the limb for an individual pixel of 30 to 40 km. Sequences of data were taken at points along the limb as viewed from the spacecraft corresponding to approximately 5° steps in latitude. The array was positioned perpendicular to the limb, with data taken for two

different placements of the array, one above the other, with approximately a 3-pixel overlap. This ensured adequate vertical coverage even in the presence of spacecraft pointing errors. For each array placement, about ten to twelve spectra were acquired per pixel with a spectral resolution of 15.5 cm^{-1} . During the time each set of spectra were taken, the instrument pointing remained essentially fixed, with the tangent points for each detector forming tight clusters in tangent height and tangent point latitude. These clusters are spaced approximately 5° in latitude and 30 to 50 km in tangent height, depending on the range of the spacecraft from Titan. In addition, spectra were taken as the array was slewed from one latitude to the next; these were excluded from the analysis. The spectra within each cluster were averaged together for each detector to improve the signal-to-noise ratio. Together, the limb maps provide fairly complete latitude coverage, but are sparse in longitude distribution as shown in Fig. 3. The characteristics of the nadir and limb data sets are listed in Tables 1 and 2, respectively.

2.2. Retrieval methodology

To retrieve information on the atmospheric temperature structure, it is necessary to formulate an appropriate radiative transfer model. If local thermodynamic equilibrium is assumed, the spectral radiance $I(\nu)$ observed at the spacecraft can be written in the form

$$I(\nu) = \int_C B[\nu, T(r, \phi, \lambda)] \frac{\partial T(\nu, s)}{\partial s} ds, \quad (1)$$

where $B(\nu, T)$ is the Planck radiance at wavenumber ν and temperature T , s is the distance from the spacecraft along the observation ray path, and $T(\nu, s)$ is the atmospheric transmittance along this distance. The atmospheric temperature field is a function of the radial distance r from the center of Titan, the latitude ϕ , and the longitude λ . For quasi-nadir observations, the integration path C extends from the surface of Titan to the spacecraft (in practice to the top of the sensible atmosphere), while for limb observations, the path passes tangentially through the atmosphere. In the absence of atmospheric refractivity, the ray paths would be linear. The spectral radiance observed by CIRS is the average from all ray paths within the solid angle of the sensor, weighted by the spatial response across the field of view. For computational expediency, we approximate this average with a single ray at the center of the field of view. Comparisons with test calculations with detailed averaging over the field of view indicate this approximation is adequate for use with the FP4 measurements used in this study.

The atmospheric transmittance appearing in (1) is an average of the monochromatic transmittance over a spectral resolution element with central wavenumber ν , weighted by the apodized spectral response function of the instrument. Specification of the transmittance requires knowledge of the absorber distributions along the ray path. Absorption in the spectral region used here is dominated by the ν_4 CH_4 band, with additional contributions by CH_3D . A stratospheric CH_4 mole fraction of 0.0141 is assumed (Niemann et al., 2005), along with a $[\text{CH}_3\text{D}]/[\text{CH}_4]$ ratio of 6.1×10^{-4} . For rapid calculation of

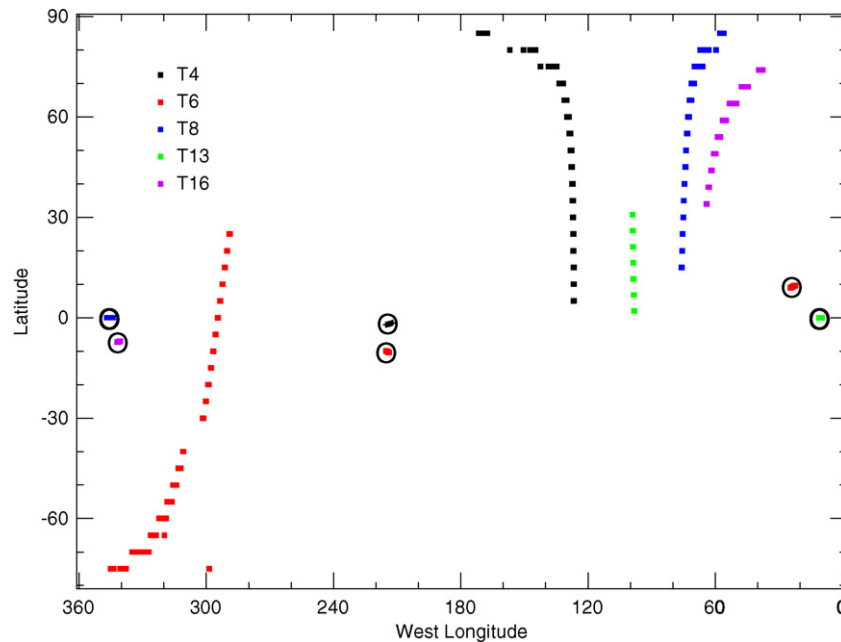


Fig. 3. Latitude and longitude of limb spectra. The circled clusters of points are the sub-spacecraft location for each observation. See Table 2 for further information.

Table 1
Summary of nadir mapping observations

Encounter	Start time	Duration	Mean longitude ($^{\circ}$ west)	Mean latitude	Resolution ($^{\circ}$ of arc)
T0	2004 Jul 02 03:30:21	13:30	356	38 $^{\circ}$ S	2.1
Tb	2004 Dec 13 15:12:29	8:25	138	07 $^{\circ}$ S	2.1
T3	2005 Feb 14 09:57:53	9:00	134	02 $^{\circ}$ S	2.1
T3	2005 Feb 15 18:57:53	4:20	356	00 $^{\circ}$ N	1.8
T4	2005 Apr 01 08:05:16	6:30	232	02 $^{\circ}$ S	1.9
T6	2005 Aug 22 20:53:37	6:47	228	13 $^{\circ}$ S	1.9
T8	2005 Oct 27 01:24:00	7:00	126	00 $^{\circ}$ N	2.9
T8	2005 Oct 28 16:15:25	7:49	340	01 $^{\circ}$ N	1.9
T9	2005 Dec 27 14:04:00	10:07	228	00 $^{\circ}$ N	2.9
T10	2006 Jan 14 14:23:27	9:13	131	00 $^{\circ}$ N	2.1
T14	2006 May 21 01:18:11	2:00	11	40 $^{\circ}$ N	1.7
T14	2006 May 21 06:18:11	2:58	358	06 $^{\circ}$ S	2.4
T15	2006 Jul 02 23:50:47	7:54	228	01 $^{\circ}$ S	2.3
T17	2006 Sep 06 21:56:51	7:20	145	07 $^{\circ}$ N	2.4
T18	2006 Sep 22 20:58:49	7:00	137	10 $^{\circ}$ N	2.3

Table 2
Summary of limb observations

Encounter	Start time	Duration	Latitude range	Mean longitude ($^{\circ}$ west)	Resolution (km)
T4	2005 Apr 01 00:25:12	3:30	3 $^{\circ}$ N–86 $^{\circ}$ N	132	35
T6	2005 Aug 22 01:10:00	2:30	34 $^{\circ}$ S–26 $^{\circ}$ N	295	35
T6	2005 Aug 22 13:40:00	2:30	80 $^{\circ}$ S–38 $^{\circ}$ S	318	35
T8	2005 Oct 27 09:38:09	3:20	11 $^{\circ}$ N–86 $^{\circ}$ N	72	40
T13	2006 Apr 30 11:53:31	5:00	1 $^{\circ}$ N–41 $^{\circ}$ N	99	28
T16	2006 Jul 22 05:25:13	2:15	31 $^{\circ}$ N–76 $^{\circ}$ N	56	33

transmittance, a correlated- k approach (Lacis and Oinas, 1991) is used, which incorporates the spectral response function of the instrument. The required molecular parameters are taken from the GEISA 2003 spectral line atlas (Jacquinet-Husson et al., 2005). Aerosols can also contribute to the atmospheric absorption as discussed further below. Once the transmittance is specified, measured radiance as a function of ν and/or ob-

servational geometry can be used to infer information on the stratospheric temperature field.

2.2.1. Limb retrieval

We first consider analysis of the limb data. The locations of the tangent points for the five limb maps used in this study are shown in Fig. 3. The encircled clusters of points represent

the sub-spacecraft locations corresponding to each sequence of measurements. In all cases, the data were taken with the spacecraft near Titan's equatorial plane. For low latitude spectra, projections of the ray paths onto the surface of Titan are essentially in the zonal direction, while at higher latitudes, the ray paths traverse a substantial range of latitudes. We anticipate that meridional temperature gradients are stronger than zonal gradients. As a consequence, the variation of temperature along a ray path associated with a low-latitude tangent point results primarily from the projection of the vertical temperature gradient onto the ray path, while at higher latitudes, both the vertical and latitude components of the gradient contribute to the variation. For the data sets used here, the latitude gradients are potentially important because of two factors. First, the ratio of the depth of Titan's atmosphere to its radius is relatively large. For a spectral region of moderate opacity, the maximum contribution to the outgoing radiance comes from a portion of the ray path centered near the tangent point with a width $\sim 2\sqrt{2r_t H}$, where H is the pressure scale height, and r_t is the distance of the tangent point from the center of Titan. For a tangent height of 200 km above Titan's surface and $H = 40$ km, this distance is ~ 670 km or a great circle arc of 20° . Second, in the spectral region near 1300 cm^{-1} and for the temperature range relevant here, the Planck radiance is very strongly dependent on T with $d \ln B / d \ln T \sim 14$, so temperature gradients along the ray path become greatly magnified. Ray paths for measurements acquired on the T4 Titan flyby, projected onto a meridional plane, are shown in Fig. 4.

In order to retrieve temperatures from these data, while properly taking into account the latitude dependence of the tem-

perature field, we have formulated a 2-dimensional (height, latitude) inversion algorithm. Work has been done previously on 2-dimensional algorithms for application to terrestrial limb-viewing thermal emission spectra. Worden et al. (2004) investigated the possibility of retrieving CO, while Steck et al. (2005) studied temperature retrieval. In both cases, feasibility studies were done using synthetic data and a geometry in which spacecraft and tangent points were in the same meridional plane. In each case, a profile of a single atmospheric parameter was retrieved with all necessary constraints assumed known, including exact pointing geometry and knowledge of the pressure field.

In formulating our limb retrieval algorithm, dependence on longitude is neglected, with the atmospheric temperature assumed to be a function of altitude and latitude only. A 2-dimensional grid is established with n layers in the vertical between Titan's surface and an altitude of 600 km with a spacing Δz in geometric height, and q latitudes with equal spacing $\Delta \phi$. Values of $n = 100$ and $\Delta \phi = 5^\circ$ are used in most cases with the value of q based on the latitude range spanned by the particular limb map used. Temperatures are defined at these grid points by the array

$$T(r_i, \phi_j) = T_{ij}; \quad i = 1, \dots, n; \quad j = 1, \dots, q. \quad (2)$$

It is necessary to first formulate a finite difference, 2-dimensional forward radiative transfer model based on (1). The ray path is divided into n_s segments, with the segment boundaries at the points where the ray path crosses altitude layer boundaries. If the distance along the ray path measured from the top of the atmosphere to the boundary between segments i and $i + 1$ is

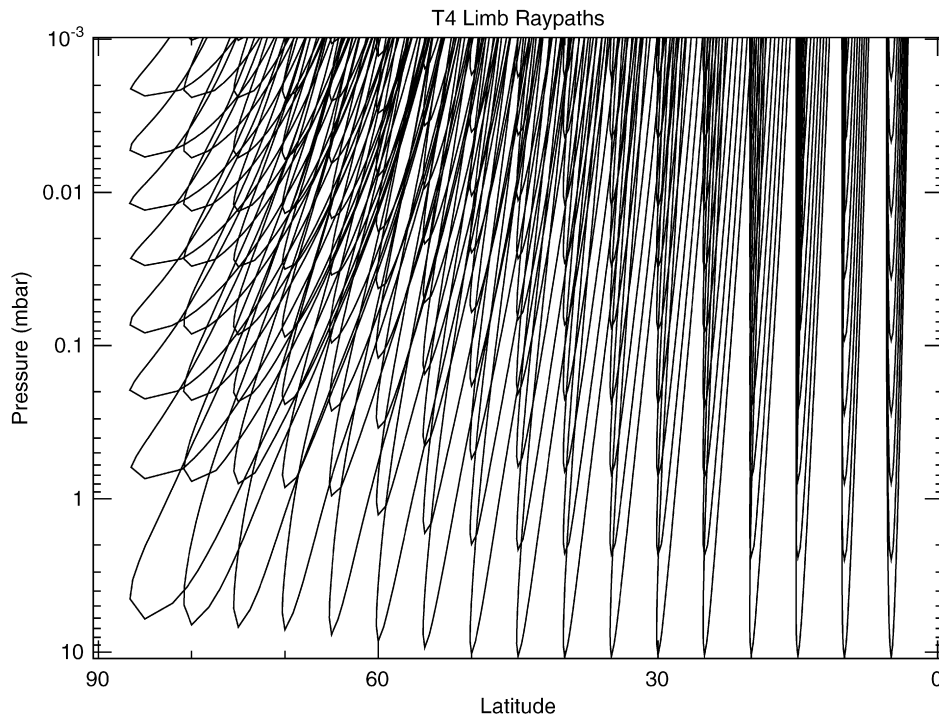


Fig. 4. Ray paths for limb measurements acquired on the T4 Titan flyby. The equatorward branch of each trajectory extends from the spacecraft to the tangent point of the ray, while the poleward branch is the extension of the ray path beyond the tangent point.

denoted by s_i , then the radiative transfer equation can be written

$$I(\nu) = \sum_{i=1}^{n_s} B(\nu, \hat{T}_i) [T(\nu, s_{i-1}) - T(\nu, s_i)]. \quad (3)$$

The temperature \hat{T}_i at the point where the ray path intersects the center of the i th layer is obtained by linear interpolation in latitude of the primary temperature array T_{ij} . To accomplish this, the latitude of the point of intersection is calculated from knowledge of the locations of the tangent point and the sub-spacecraft point. It is assumed that refraction of the ray path can be neglected. Estimates indicate that at a tangent height of 150 km, for example, the actual ray path near the tangent point is refracted downward by only ~ 10 m relative to the adopted linear path. The latitude of each point along the ray path can be calculated by noting that the ray path projection on a reference sphere centered on Titan follows a great circle passing through both the sub-spacecraft and the tangent point locations. The meridional ray path projections shown in Fig. 4 were obtained in this way.

Calculation of the transmittances in (3) requires a knowledge of the distribution of absorbers along the ray path. The distributions of CH_4 and CH_3D can be obtained from their mole fractions, providing the pressure and temperature along the ray path are known. The pressure profile at each latitude grid point is obtained by integration of the hydrostatic equation. This requires knowledge of pressures at each latitude on a reference surface of constant gravitational potential, along with the temperature profile at all levels between the reference surface and the top of the atmospheric model. An interpolation of the pressure in latitude for each point along the ray path is carried out similar to that used for temperatures. An alternative formulation could be developed using a pressure-related vertical coordinate such as $-\ln p$. However, it is still necessary to invoke the hydrostatic equation, along with the appropriate boundary conditions, to relate the pressure field to the geometry of the limb tangent observations.

Aerosols may also contribute significant absorption with the long paths associated with the limb tangent geometry. We assume the aerosols can be treated as pure absorbers, and specify profiles of $(d\tau_a/dr)_{ij}$ at each grid point where τ_a is the normal aerosol optical depth, taken to be independent of wavenumber over the spectral region used here. Again, interpolation in latitude is used to specify this quantity at each required point along the ray path.

We now turn to the development of an appropriate retrieval algorithm. Radiances from eight spectral points spaced 15 cm^{-1} apart between 1210 and 1315 cm^{-1} are used in the retrievals, providing a sampling of the widest range of atmospheric opacity available in this spectral region with this spectral resolution.

Since both the temperature and aerosol distributions are unknown, it is necessary to attempt to retrieve both parameters from the measurements. In addition, we also infer a single shift ξ_l in all tangent heights at a given tangent point latitude $(\phi_t)_l$ ($l = 1, \dots, p$). The reason for this is two-fold. First, the tangent heights provided in the data sets can be incorrect

because of errors in knowledge of the spacecraft orientation. Second, the pressure is not precisely known on a constant gravitational potential surface nor are necessary portions of the temperature profile which may lie outside the region for which information can be retrieved from the measurements. Inference of ξ_l attempts to compensate for both of these effects by properly aligning the tangent heights with the pressure field.

In practice, offsets to the tangent point altitude can have a very similar affect on the spectrum as scaling the aerosol optical depth profile, so that there can be an ambiguity between the retrieved values for the tangent height correction and aerosol optical depth. Therefore, although we retrieve aerosol optical depth profiles along with the temperature, we do not present the retrieved aerosol profiles in this paper. We have examined the effect of the aerosol opacity on our temperature retrievals by also performing temperature retrievals assuming no aerosol opacity, using a more restricted wavenumber range (1270 to 1300 cm^{-1}) where the effect of the aerosol on the spectrum is lowest. Results from the temperature only retrievals typically differ from the combined temperature and aerosol retrievals by up to about 1 K over the altitude range where the retrievals are valid.

Spectra with 0.5 cm^{-1} resolution would give better access to the continuum between gaseous absorption lines, permitting better separation of the retrieved aerosol profile and tangent height shift. Averages of 0.5 cm^{-1} limb spectra at 15° S and 85° N have been successfully inverted by [Vinatier et al. \(2007\)](#) to obtain temperature, gas abundances, and aerosol opacity. Because of the relatively large amount of integration time required to obtain an adequate signal-to-noise ratio, extensive spatial coverage is not possible with this high-resolution mode. Since spectra taken at 15 cm^{-1} resolution provide good signal-to-noise in a relatively short time, this observing mode was used in limb temperature maps where good latitude coverage was desired.

Two approaches to the 2-dimensional inversion problem were examined. In the first, the 2-dimensional forward model is used, but retrievals are carried out at each tangent point latitude individually, progressing from low to high latitudes. At a given latitude, only temperatures at that latitude are retrieved, with temperatures along the ray paths at all lower latitudes specified from the previous retrievals. Temperatures poleward of the tangent point latitude are obtained by extrapolation. This approach takes advantage of the fact that the ray paths at low latitudes are primarily zonal, and coupling in latitude gradually increases moving poleward. In the second approach, atmospheric parameters at all latitudes are retrieved simultaneously from the entire set of measurements. The two methods were found to give similar results. Only the second approach will be considered further here.

The measured spectral radiance is a function of ν , r_t , and ϕ_t . For convenience, these measurements are incorporated into a single m -element vector \mathbf{y} whose elements are the radiances corresponding to the sets $[\nu, r_t, \phi_t]_k$ ($k = 1, \dots, m$). For the larger limb sequences, m exceeds 1000. In a similar fashion, we can construct a single vector \mathbf{x} containing all of the quantities to be retrieved. Define the sets of vectors \mathbf{T}_j and \mathbf{b}_j

($j = 1, \dots, q$) representing the columns of the arrays T_{ij} and $\ln(d\tau_c/dr)_{ij}$, respectively. These n -element vectors represent the vertical temperature and aerosol profiles at the j th latitude grid point. Combining these vectors with the tangent point shifts ξ_l ($l = 1, \dots, p$) we obtain

$$\mathbf{x} = \begin{bmatrix} \mathbf{T}_1 \\ \vdots \\ \mathbf{T}_q \\ \mathbf{b}_1 \\ \vdots \\ \mathbf{b}_q \\ \xi_1 \\ \vdots \\ \xi_p \end{bmatrix}. \quad (4)$$

A forward spectral radiance model vector $\mathbf{f}(\mathbf{x})$ with m -elements is defined such that the k th element is the spectral radiance calculated using (3) for the set $[\nu, r_t, \phi_t]_k$. The sensitivities of the radiances to the temperature and aerosol profiles at the j th latitude grid point can be written as the $m \times n$ Jacobian matrices

$$\mathbf{L}_j = \frac{\partial \mathbf{f}}{\partial \mathbf{T}_j}; \quad j = 1, \dots, q, \quad (5)$$

$$\mathbf{M}_j = \frac{\partial \mathbf{f}}{\partial \mathbf{b}_j}; \quad j = 1, \dots, q. \quad (6)$$

These partial derivatives are calculated analytically from the discretized forward model. The partial derivatives of the radiances with respect to the shifts in tangent height at each tangent point latitude can be written as a set of m -element vectors

$$\mathbf{u}_l = \frac{\partial \mathbf{f}}{\partial \xi_l}; \quad l = 1, \dots, p, \quad (7)$$

and are calculated by numerical perturbation. The matrices (5) and (6) along with the vectors (7) can be combined into a single array \mathbf{K} of dimensions $m \times (2nq + p)$, which can be written in block form

$$\mathbf{K} = [\mathbf{L}_1 \cdots \mathbf{L}_q \quad \mathbf{M}_1 \cdots \mathbf{M}_q \quad \mathbf{u}_1 \cdots \mathbf{u}_p]. \quad (8)$$

The forward model $\mathbf{f}(\mathbf{x})$ can be expanded about a reference set of atmospheric parameters \mathbf{x}^0 , which to first order can be written

$$\mathbf{f}(\mathbf{x}) = \mathbf{f}(\mathbf{x}^0) + \mathbf{K}\Delta\mathbf{x}, \quad (9)$$

where

$$\Delta\mathbf{x} = \mathbf{x} - \mathbf{x}^0. \quad (10)$$

We proceed to formulate a constrained inversion algorithm by minimizing the penalty function

$$Q = (\Delta\mathbf{y} - \mathbf{K}\Delta\hat{\mathbf{x}})^T \mathbf{E}^{-1} (\Delta\mathbf{y} - \mathbf{K}\Delta\hat{\mathbf{x}}) + \Delta\hat{\mathbf{x}}^T \mathbf{S}^{-1} \Delta\hat{\mathbf{x}}, \quad (11)$$

where $\Delta\mathbf{y} = \mathbf{y} - \mathbf{f}(\mathbf{x}^0)$ with \mathbf{y} the measured radiance, \mathbf{E} is the measurement error covariance matrix, and $\hat{\mathbf{x}} = \mathbf{x}^0 + \Delta\hat{\mathbf{x}}$ is the constrained solution sought. Under the assumption that the random errors in the m measurements are uncorrelated,

the error covariance matrix is assumed to be diagonal, with values equal to the square of the noise equivalent spectral radiance (NESR) of each measurement. Matrix transposition is denoted by the superscript T . The first term in (11) is χ^2 , as used in standard least squares estimation, while the second term represents a constraint that must be included to obtain a physically meaningful solution from the ill-posed problem. The matrix \mathbf{S} is determined by the specific constraints chosen. The penalty function Q is similar in form to that frequently employed in 1-dimensional inversion problems, and minimization is straight forward (see, for example, Press et al., 1994; Rodgers, 2000), yielding

$$\Delta\hat{\mathbf{x}} = \mathbf{S}\mathbf{K}^T \mathbf{H}^{-1} \Delta\mathbf{y}, \quad (12)$$

where

$$\mathbf{H} = (\mathbf{K}\mathbf{S}\mathbf{K}^T + \mathbf{E}). \quad (13)$$

The matrix \mathbf{H} is large ($m \times m$), but its inversion is accomplished efficiently using Cholesky decomposition and back substitution (see, for example, Press et al., 1994). Because of the nonlinear dependence of the measurements on the atmospheric parameters, it is necessary to iterate the solution. Note that we do *not* constrain the final solution to necessarily lie near the reference value \mathbf{x}^0 —since we have little *a priori* knowledge of Titan's thermal structure and aerosol distribution, at each iteration we replace \mathbf{x}^0 with the \mathbf{x} from the previous iteration.

The constraint matrix \mathbf{S} is chosen to permit filtering of the retrieved temperature and aerosol fields in both height and latitude. This is accomplished by imposing correlations of the profiles between atmospheric levels at each grid point latitude and correlations between latitudes at each atmospheric level. Correlations between latitudes for the retrieved tangent height shifts are also included. \mathbf{S} can be displayed schematically in block form

$$\mathbf{S} = \begin{bmatrix} \mathbf{U}_{11} & \cdots & \mathbf{U}_{1q} & \mathbf{O} & \cdots & \mathbf{O} & \mathbf{O} & \cdots & \mathbf{O} \\ \vdots & & \vdots & \vdots & & \vdots & \vdots & & \vdots \\ \mathbf{U}_{1q} & \cdots & \mathbf{U}_{qq} & \mathbf{O} & \cdots & \mathbf{O} & \mathbf{O} & \cdots & \mathbf{O} \\ \mathbf{O} & \cdots & \mathbf{O} & \mathbf{V}_{11} & \cdots & \mathbf{V}_{1q} & \mathbf{O} & \cdots & \mathbf{O} \\ \vdots & & \vdots & \vdots & & \vdots & \vdots & & \vdots \\ \mathbf{O} & \cdots & \mathbf{O} & \mathbf{V}_{1q} & \cdots & \mathbf{V}_{qq} & \mathbf{O} & \cdots & \mathbf{O} \\ \mathbf{O} & \cdots & \mathbf{O} & \mathbf{O} & \cdots & \mathbf{O} & w_{11} & \cdots & w_{1p} \\ \vdots & & \vdots & \vdots & & \vdots & \vdots & & \vdots \\ \mathbf{O} & \cdots & \mathbf{O} & \mathbf{O} & \cdots & \mathbf{O} & w_{1p} & \cdots & w_{pp} \end{bmatrix}, \quad (14)$$

where null matrices of appropriate dimensions are represented by the \mathbf{O} symbols, and the $\mathbf{U}_{jj'}$ are $n \times n$ matrices which impose 2-point correlation in the vertical as well as between grid point latitudes ϕ_j and $\phi_{j'}$. The form chosen is

$$\mathbf{U}_{jj'} = \alpha_z \mathbf{C} \delta_{jj'} + \alpha_\phi \mathbf{I}_n D_{jj'}; \quad j, j' = 1, \dots, q, \quad (15)$$

where the $n \times n$ matrix \mathbf{C} specifies the correlation in the vertical at a given latitude, and $D_{jj'}$ is the correlation in latitude at a given height. \mathbf{I}_n is an $n \times n$ unit matrix, and the scalars α_z and α_ϕ determine the strength of the filtering. Adopting Gaussian

correlation filters,

$$C_{ii'} = \exp[-(i - i')^2 \Delta z^2 / 2c_z^2]; \quad i, i' = 1, \dots, n, \quad (16)$$

where c_z is the vertical correlation length or filter width. The filter in latitude is

$$D_{jj'} = \exp[-(j - j')^2 \Delta \phi^2 / 2c_\phi^2]; \quad j, j' = 1, \dots, q, \quad (17)$$

where c_ϕ is the latitude correlation length. The matrices $\mathbf{V}_{jj'}$ provide similar filtering on the aerosol field and are written

$$\mathbf{V}_{jj'} = \beta_z \mathbf{C} \delta_{jj'} + \beta_\phi \mathbf{I}_n D_{jj'}; \quad j, j' = 1, \dots, q. \quad (18)$$

Smoothing in latitude of the tangent height shifts is accomplished using

$$w_{ll'} = \gamma_\phi \exp[-(l - l')^2 \Delta \phi_l^2 / 2c_\phi^2]; \quad l, l' = 1, \dots, p, \quad (19)$$

where $\Delta \phi_l$ is the characteristic tangent point latitude spacing of 5° .

A vertical correlation length $c_z = 40$ km was used, and the latitude correlation length c_ϕ was set equal to the latitude grid spacing. The parameters α_z , α_ϕ , β_z , β_ϕ , and γ_ϕ were determined empirically to yield stable solutions, which are also consistent with $\chi^2 \sim m$.

Using (13)–(19) in the solution (12), and explicitly displaying the retrieved temperature and aerosol profiles for each grid point latitude, we obtain

$$\Delta \hat{\mathbf{T}}_j = \left[\sum_{j'=1}^q \mathbf{U}_{jj'} \mathbf{L}_{j'}^T \right] \mathbf{H}^{-1} \Delta \mathbf{y}; \quad j = 1, \dots, q \quad (20)$$

and

$$\Delta \hat{\mathbf{b}}_j = \left[\sum_{j'=1}^q \mathbf{V}_{jj'} \mathbf{M}_{j'}^T \right] \mathbf{H}^{-1} \Delta \mathbf{y}; \quad j = 1, \dots, q. \quad (21)$$

The solution for the shift in tangent height is

$$\xi_l = \left[\sum_{l'=1}^p w_{ll'} \mathbf{u}_{l'}^T \right] \mathbf{H}^{-1} \Delta \mathbf{y}; \quad l = 1, \dots, p. \quad (22)$$

The random error in the retrieved temperature profile resulting from the propagation of random error in the measured radiances can be calculated from (20). The resulting retrieved temperature error covariance matrices for the profile at grid point latitudes ϕ_j and $\phi_{j'}$ become

$$\mathbf{R}_{jj'} = \left[\sum_{j''=1}^q \mathbf{U}_{jj''} \mathbf{L}_{j''}^T \right] \mathbf{H}^{-1} \mathbf{E} \mathbf{H}^{-1} \left[\sum_{j''=1}^q \mathbf{L}_{j''} \mathbf{U}_{j''j'} \right]; \quad j, j' = 1, \dots, q. \quad (23)$$

In this expression, we have made use of the fact \mathbf{C} and \mathbf{H} are symmetric matrices. In the present analysis, we are interested only in the diagonal elements of the $n \times n$ matrices \mathbf{R}_{jj} , which represent the error variance at each atmospheric level for the profile at latitude ϕ_j . The error covariance matrices for the retrieved aerosol profiles are similar in form to (23).

To investigate the behavior of the 2-dimensional retrieval algorithm outlined above, we have applied it to synthetic

measurements. Examples are shown in Figs. 5 and 6. Spectral radiances were calculated using our 2-D forward model, assuming an observation geometry corresponding to the T4 limb map. Two different model temperature cross-sections were used, one with a relatively warm upper atmosphere at high latitudes and the other with a cold polar region. Random noise was added to the radiances with a rms value of $3 \times 10^{-10} \text{ W cm}^{-2} \text{ ster}^{-1} / \text{cm}^{-1}$, which is approximately the effective Noise Equivalent Spectral Radiance (NESR) for the averages of ~ 10 spectra as used in the limb map retrievals. As a basis for comparison, retrievals were first carried out using a 1-dimensional inversion algorithm, treating the data at each limb point latitude independently and assuming horizontal homogeneity (Figs. 5 and 6, top). At the higher northern latitudes, there are substantial errors in the retrieved cross-sections because of the inability of the 1-dimensional retrieval to distinguish between latitude and height components of the temperature gradients. The 2-dimensional retrieval algorithm yields substantially better results in both cases (Figs. 5 and 6, bottom). As the edges of the retrieval domain are approached both vertically and horizontally, the information content decreases, and the retrieved thermal structure becomes increasingly less well constrained. This accounts for the deterioration in the quality of the 2-dimensional retrieval at the northernmost latitudes and higher atmospheric levels. For this reason, in the analyses that follow we will not use retrieved temperatures from limb measurements poleward of 75° N nor for pressures less than 0.005 mbar.

2.2.2. Nadir retrieval

Inversion of the nadir-viewing spectra is accomplished with a 1-dimensional retrieval algorithm of a type extensively discussed previously (Conrath et al., 1998). In this case $\hat{z} = -\ln p$ is used as the vertical coordinate. A vertical temperature profile is retrieved from each individual spectrum. Minimization of a penalty function analogous to (11) gives

$$\Delta \hat{\mathbf{T}} = \mathbf{S} \mathbf{K}^T (\mathbf{K} \mathbf{S} \mathbf{K}^T + \mathbf{E})^{-1} \Delta \mathbf{I} \quad (24)$$

and, for the 1-dimensional retrieval, \mathbf{K} and \mathbf{S} are, in component form,

$$K_{ki} = \frac{\partial B[v_k, T(\hat{z}_i)]}{\partial T} \frac{\partial T(v_k, \hat{z}_i)}{\partial \hat{z}}; \quad k = 1, \dots, m; \quad i = 1, \dots, n, \quad (25)$$

and

$$S_{ii'} = \alpha_z \exp[-(i - i')^2 \Delta \hat{z}^2 / c_z^2]; \quad i, i' = 1, \dots, n, \quad (26)$$

where $\Delta \hat{z}$ is the vertical layer increment, c_z is vertical correlation length (usually chosen to be 1 pressure scale height), and α_z controls the strength of the vertical filter. $\Delta \mathbf{I}$ is the difference between the measured spectral radiance and that calculated with the forward model, using the reference temperature profile \mathbf{T}^0 . The retrieved vertical temperature profile is

$$\hat{\mathbf{T}} = \mathbf{T}^0 + \Delta \hat{\mathbf{T}}. \quad (27)$$

As in the 2-dimensional limb case, the non-linearity of the problem requires iteration.

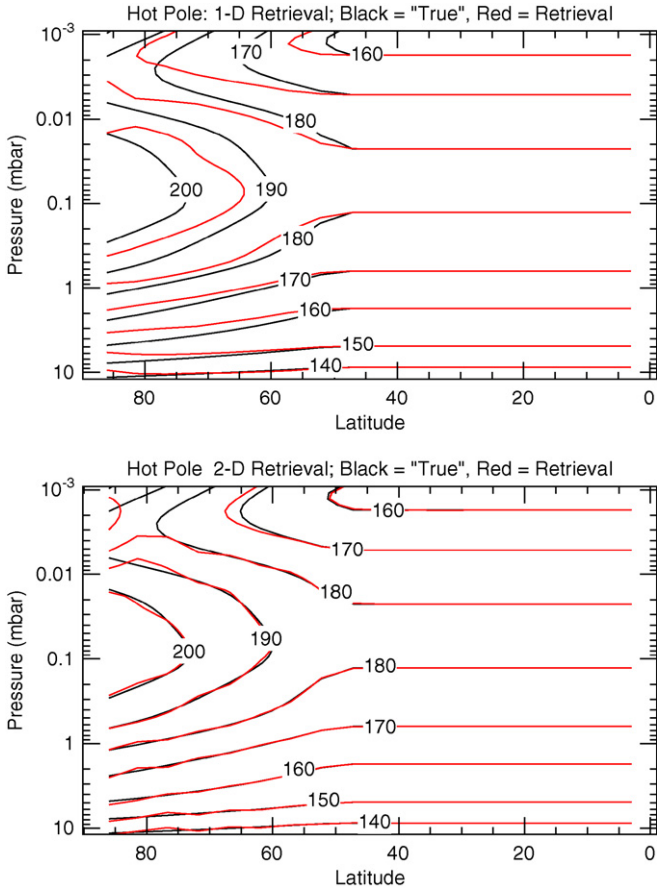


Fig. 5. One- and two-dimensional retrieval results on synthetic data with a warm pole, as discussed in the text. The one-dimensional retrieval does not recover the polar warm spot well.

Because of Titan's relatively thick atmosphere, the latitude and longitude of points along the ray path at higher atmospheric levels can differ significantly from the coordinates of the point of intersection of the ray path with Titan's surface, especially for data taken at large emission angles. Consequently, the retrieved temperature profile is not strictly representative of the local vertical thermal structure when horizontal temperature gradients are present. Rather than attempting a full 2-dimensional nadir retrieval as was done with the limb data, a correction is introduced by calculating the latitude and longitude associated with each atmospheric level along the ray path. These level-dependent coordinates are used in constructing the cross-sections and maps discussed in the following sections.

3. Results

The first step in our analysis of the retrieved temperatures is to calculate a zonal mean meridional cross-section. We use a combination of nadir and limb retrievals for this purpose. The inversion algorithms discussed in the previous section were applied to all of the data sets listed in Table 1, using as an initial guess temperature profile the 15° S profile from Flasar et al. (2005).

The pressure range over which useful information on the temperature structure is obtained from the nadir data depends

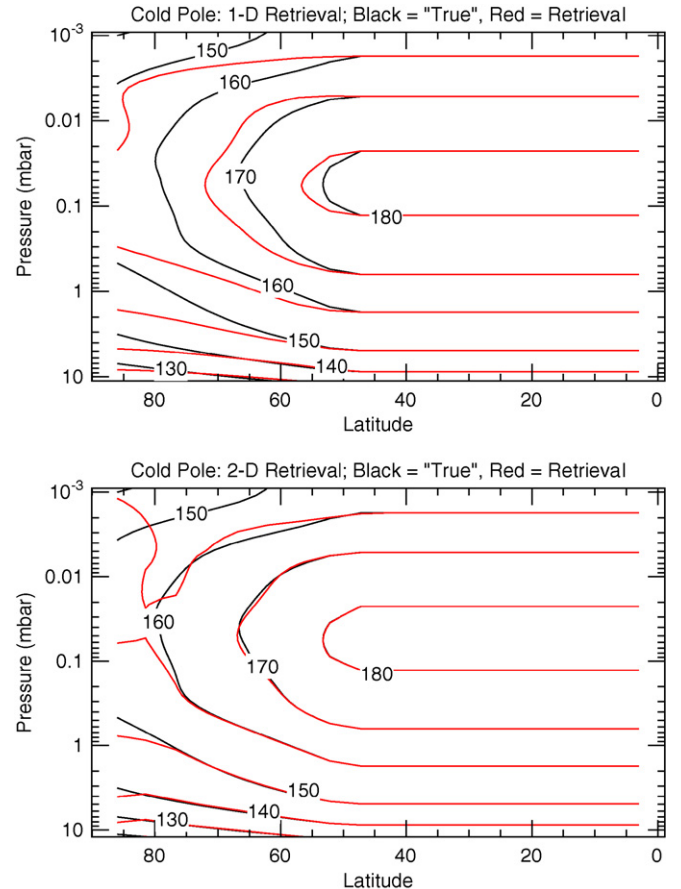


Fig. 6. One- and two-dimensional retrieval results on synthetic data with a cold pole, as discussed in the text.

on both the emission angle of the observations and the thermal structure itself, being more heavily weighted toward warm regions. The temperature variance resulting from the propagation of random measurement error serves as an indicator of the relative information content. Fig. 7 shows a meridional cross-section of the square root of the error variance, calculated using the 1-dimensional nadir equivalent of (23). In regions where there is strong sensitivity of the measured radiances to the thermal structure, the error variance is relatively low. The error increases moving toward both lower and higher pressures until maxima are reached. Finally, as the sensitivity decreases further at the both the lowest pressures and deepest levels, the error once again decreases. In these regions, the algorithm retrieves values approaching the reference profile, but does so with high precision. Thus, the upper and lower maxima of the estimated error provide bounds for the region of useful information on the thermal structure. A similar error cross-section for the limb retrievals is shown in Fig. 8. In this case, the full 2-dimensional version of (23) was used. These results indicate that the nadir retrievals give useful results from approximately 0.2 to 5 mbar, except at high northern latitudes where the deep pressure limit decreases to ~2 mbar. Inclusion of the limb results moves the lower pressure limit approximately two decades to ~0.003 mbar.

A composite mean meridional temperature cross-section was constructed, using all of the nadir and limb maps. The

temperatures at each pressure level were averaged in 5° latitude bins, and the resulting averages were then smoothed with three passes of a sliding 10° rectangular window. For pressures greater than ~ 0.2 mbar, the averages are dominated by the nadir retrievals, which provide good sampling in longitude at most latitudes. However, they are distributed over an approximately 2-year time interval as indicated in Table 1. At lower pressures, the results depend predominately on the limb retrievals, with extremely limited coverage in longitude (see Fig. 3). Because of these limitations, the results should be regarded as representative of the large scale meridional structure at this particular season rather than as a detailed zonal mean meridional cross-section for a given point in time. The resulting temperatures are shown in Fig. 9. For pressures greater than ~ 0.5 mbar, the

temperatures are consistent with the preliminary, nadir-only results of Flasar et al. (2005) with the warmest temperatures at the equator, and much larger gradients in the northern (winter) hemisphere than in the southern hemisphere. At lower pressures, seen only with the limb observations, we find that the stratopause is almost 20 K warmer and a decade lower in pressure at high northern latitudes than at the equator and in the southern hemisphere. At 10° S, our retrieved temperatures are up to 10 K colder than the temperatures measured by the Huygens Atmospheric Structure Instrument (HASI) in the upper stratosphere between 0.1 and 1 mbar (Fulchignoni et al., 2005). Conversely, synthetic spectra calculated using the HASI measured temperature profile have radiances in the ν_4 CH_4 band that are over 30% larger than the radiances measured by CIRS. The reason for the discrepancy between the two instruments is currently unknown.

Using the assumption that the meridional pressure gradient is balanced by the sum of the horizontal components of the Coriolis and centrifugal forces, which is expected to hold for Titan, the zonal wind velocity u is related to the meridional temperature gradient through the gradient wind equation

$$\frac{\partial}{\partial z_{\parallel}} \left(2\Omega u + \frac{u^2}{r \cos \phi} \right) = -\frac{g}{T} \frac{1}{r} \left(\frac{\partial T}{\partial \phi} \right)_p, \quad (28)$$

where Ω is the rotation rate of Titan, ϕ is latitude, g is gravitational acceleration, and for a thick atmosphere, the “vertical” derivative is taken along cylinders parallel to the rotation axis (see, for example, Flasar et al., 2005). To calculate a wind velocity from (28), it is necessary to specify a boundary condition. Currently, few constraints on the wind field exist. We have chosen to assume solid-body rotation at the 10 mbar level at an angular velocity of four times Titan’s solid-body rotation rate, consistent with the Huygens Doppler Wind Experiment measurements at that altitude (Bird et al., 2005;

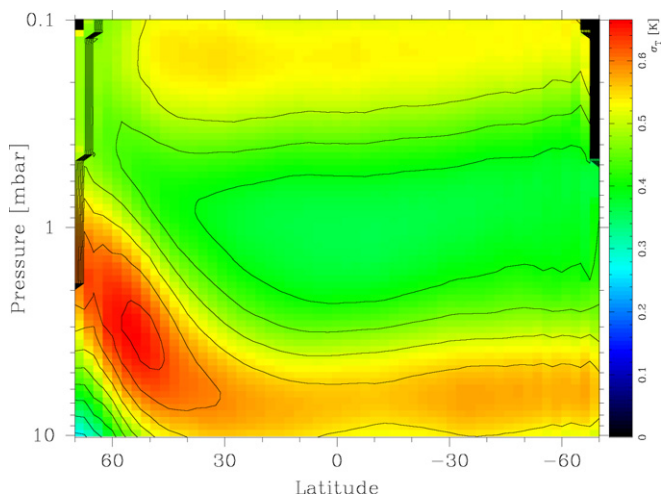


Fig. 7. Uncertainty in temperatures retrieved from a single spectrum, from nadir data from the T4 flyby, resulting from propagation of random errors in the measured radiances.

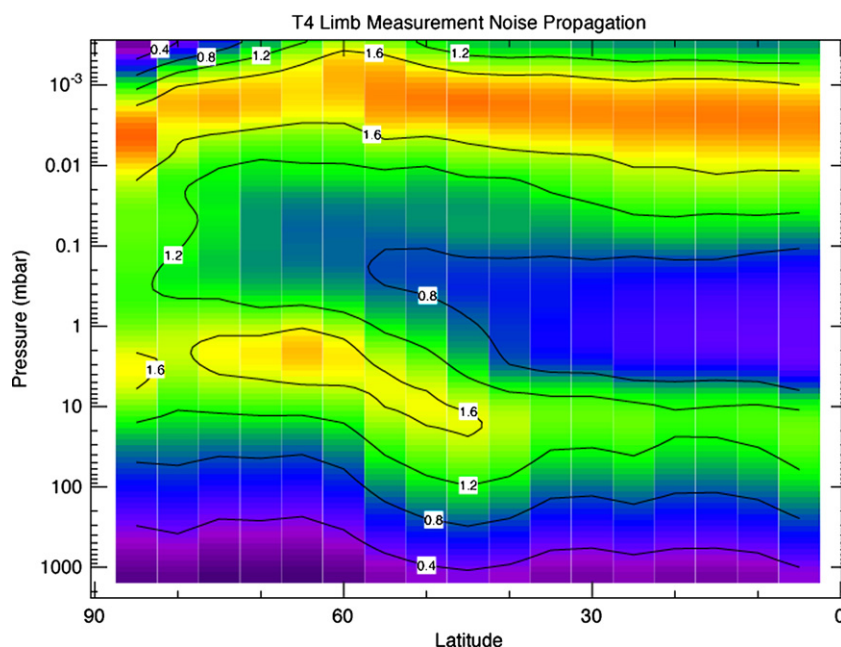


Fig. 8. Uncertainty in temperatures retrieved from limb data from the T4 flyby, resulting from propagation of random errors in the measured radiances.

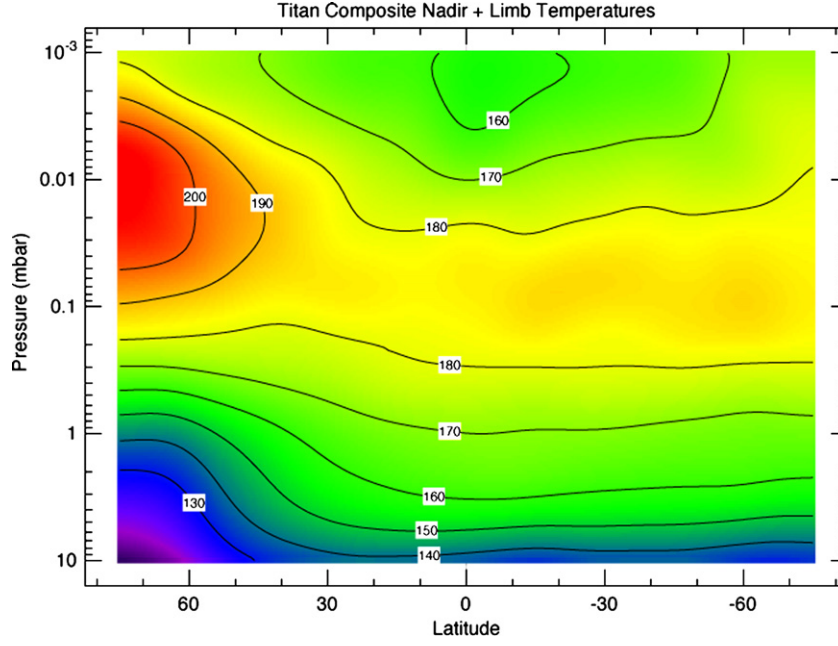


Fig. 9. Zonal mean temperatures from all limb and nadir maps. Retrieved temperatures were averaged in 5° latitude bins, then smoothed with a 10° boxcar function applied three times. Contours are labeled in K.

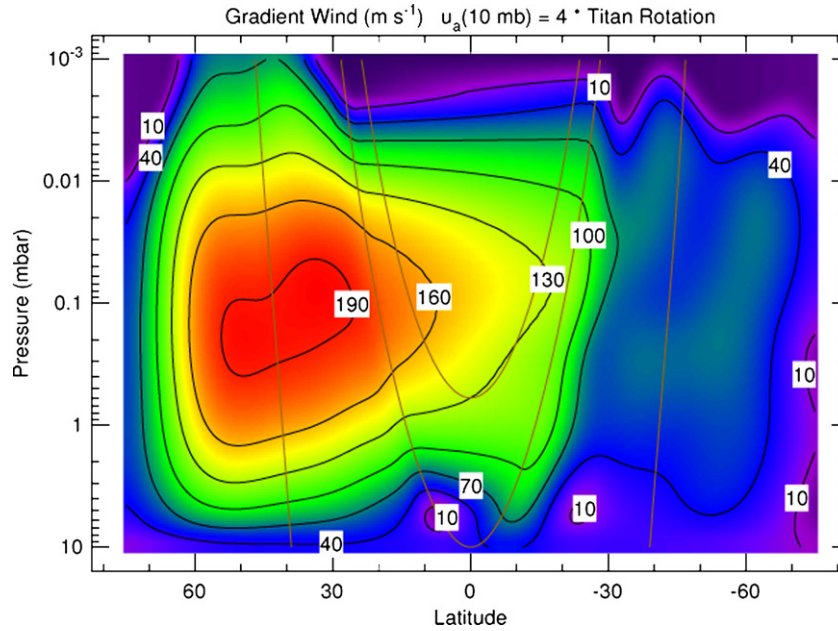


Fig. 10. Zonal winds calculated from the temperatures in Fig. 9 from the gradient wind equation, assuming solid-body rotation at the 10 mbar level at four times Titan's rotation rate. Wind speed contours (black lines) are labeled in m s^{-1} . The gray lines indicate cylindrical surfaces parallel to the rotation axis along which the gradient wind equation is integrated. Equatorward and above the gray line tangent to the equator at 10 mbar, the winds are unconstrained by the gradient wind equation, and have been linearly interpolated on constant pressure surfaces.

Folkner et al., 2006). The resulting wind cross-section is shown in Fig. 10. Equatorward and above the line defining the cylinder tangent to the equator at 10 mbar, the wind field is unconstrained by (28), and u has been linearly interpolated on constant pressure surfaces. The resulting wind profile has a single strong jet at northern midlatitudes, with peak winds of about 190 m s^{-1} between 30° N and 50° N at a pressure of 0.01 mbar.

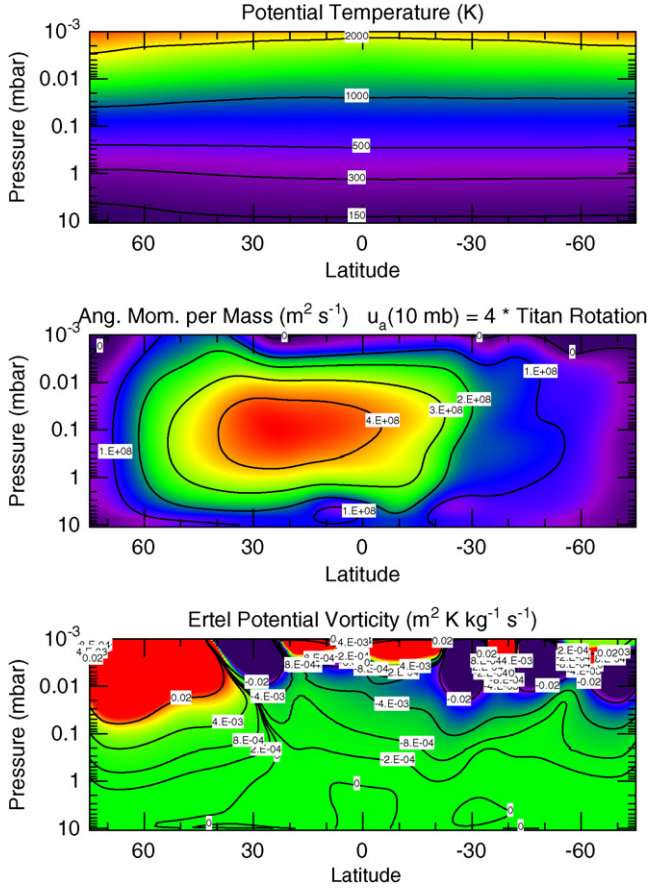
From the calculated zonal mean winds, we can also estimate the zonal mean angular momentum per unit mass

$$M = (\Omega r \cos \phi + \bar{u})r \cos \phi, \quad (29)$$

and the zonal mean of the Ertel potential vorticity

$$\bar{Q} = \frac{\vec{\nabla} \times \vec{v} \cdot \vec{\nabla} \theta}{\rho} = -g \frac{1}{a^2 \cos \phi} \left(\frac{\partial \theta}{\partial \phi} \bigg|_p \frac{\partial M}{\partial p} - \frac{\partial \theta}{\partial p} \frac{\partial M}{\partial \phi} \bigg|_p \right), \quad (30)$$

which is a conserved quantity for adiabatic, frictionless motion. Here \vec{v} is the velocity vector, and θ is the potential temperature.



the radius of Titan as the horizontal scale L gives an estimate of the magnitude of the meridional velocity of $\bar{v} \sim 3 \text{ cm s}^{-1}$. The estimated velocities also allow us to determine a dynamical timescale for the meridional circulation $t_{\text{dyn}} = H/\bar{w} = L/\bar{v} \approx 9 \times 10^7 \text{ s}$ (about 3 years), about three times larger than the radiative timescale but still somewhat shorter than the seasonal timescales.

Given the meridional velocity scale, we can then estimate the order of magnitude of the EP flux divergence near the center of the observed jet where the spatial derivatives of the zonal velocity can be ignored, and assuming that the time derivative of the zonal velocity is also small. With these assumptions,

$$\frac{1}{\rho_0 a \cos \phi} \nabla \cdot \mathbf{F} = \bar{v} \left(\frac{\bar{u} \tan \phi}{a} - f \right), \quad (36)$$

which gives us $\nabla \cdot \mathbf{F}/(a\rho_0) \sim 2 \times 10^{-6} \text{ m s}^{-2}$ at northern mid-latitudes, giving a timescale of $\sim 9 \times 10^7 \text{ s}$ for the eddy forcing of the mean zonal flow. Flasar and Conrath (1990) first calculated that the dynamical timescales on Titan are significantly longer than the thermal timescale, based on Voyager IRIS observations. They pointed out that, because of the coupling of the temperature and winds through gradient wind balance, the stratospheric temperatures will lag the thermal forcing by more than would be expected simply from the thermal timescale.

4.2. Winter stratospheric jet

The zonal mean wind structure implied by the observed temperatures (Fig. 10) is dominated by a single strong jet in the middle stratosphere at northern midlatitudes, with only weak winds in the southern hemisphere. The meridional structure of the zonal mean winds is consistent with wind measurements from the November 2003 stellar occultations by Sicardy et al. (2006). Thermal infrared observations by Voyager, just after the northern spring equinox, also showed strong winds at mid-northern latitudes, albeit considerably weaker than the Cassini data ($\sim 80 \text{ m s}^{-1}$) and with strong winds ($\sim 60 \text{ m s}^{-1}$) also at high southern latitudes (Flasar and Conrath, 1990). Analysis of the 28 Sgr stellar occultation, during early northern summer, showed a very strong jet ($\sim 175 \text{ m s}^{-1}$) in the southern hemisphere, but the data was not sensitive to winds in the northern hemisphere (Hubbard et al., 1993; Sicardy et al., 1999). Despite the sparse temporal coverage, there is an apparent pattern of a strong jet in the winter hemisphere, forming during the fall and dissipating sometime after the spring equinox.

Poleward of the winter hemispheric jet, temperatures in the lower stratosphere are at least 25 K colder than at the equator, whereas the stratopause is roughly 20 K warmer than at the equator and is elevated by about two scale heights. Composition determinations from CIRS data also show a strong enhancement in the abundance of nitriles and some trace hydrocarbons at latitudes within and poleward of the jet (Teanby et al., 2006, 2007; Coustenis et al., 2007; Vinatier et al., 2007). The enhancement of nitriles was also seen by Voyager (Coustenis and Bézard, 1995), indicating that the enhancement persists into early spring.

The structure of Titan's winter polar stratosphere is remarkably similar in many respects to the winter polar vortex on Earth—a strong jet in the stratosphere which forms in autumn and decays in spring surrounding and isolating a polar stratosphere with anomalous composition—enhanced nitriles on Titan, depleted CH_4 and N_2O and enhanced HF on Earth (Abrams et al., 1996a, 1996b)—and an elevated polar stratopause. In the terrestrial winter polar stratosphere, the elevated, warm stratopause is caused by downward motion driven by drag from breaking gravity waves (Hitchman et al., 1989), while the composition is determined by a combination of the downward motion and meridional mixing by planetary waves (Bacmeister et al., 1996). Models of Titan's atmosphere by Hourdin et al. (2004) indicate that a similar process can explain the enhancement of HCN in Titan's winter polar stratosphere. With higher polar altitudes in permanent sunlight, and the increased aerosol abundance in the winter polar hood, heating from absorption of sunlight by aerosols may also contribute to the warm polar stratopause.

Acknowledgments

We thank M.E. Segura, M.H. Elliott, J.S. Tingley, S. Albright, E. Lellouch and P.N. Romani for their work on CIRS instrument commanding, D.E. Jennings, A. Mamoutkin, R. Carlson and V. Kunde for data calibration, and P.J. Schinder for calculating pointing information. This work has been supported by the NASA Cassini Project and by the NSF Planetary Astronomy Program.

References

- Abrams, M.C., Manney, G.L., Gunson, M.R., Abbas, M.M., Chang, A.Y., Goldman, A., Irion, F.W., Michelsen, H.A., Newchurch, M.J., Rinsland, C.P., Salawitch, R.J., Stiller, G.P., Zander, R., 1996a. ATMOS/ATLAS-3 observations of long-lived tracers and descent in the Antarctic vortex in November 1994. *Geophys. Res. Lett.* 23, 2341–2344.
- Abrams, M.C., Manney, G.L., Gunson, M.R., Abbas, M.M., Chang, A.Y., Goldman, A., Irion, F.W., Michelsen, H.A., Newchurch, M.J., Rinsland, C.P., Salawitch, R.J., Stiller, G.P., Zander, R., 1996b. Trace gas transport in the Arctic vortex inferred from ATMOS ATLAS-2 observations during April 1993. *Geophys. Res. Lett.* 23, 2345–2348.
- Andrews, D.G., Holton, J.R., Leovy, C.B., 1987. *Middle Atmosphere Dynamics*. Academic Press, Orlando.
- Bacmeister, J.T., Schoeberl, M.R., Summers, M.E., Rosenfield, J.R., Zhu, X., 1996. Descent of long-lived trace gases in the winter polar vortex. *J. Geophys. Res.* 100, 11669–11684.
- Bird, M.K., Allison, M., Asmar, S.W., Atkinson, D.H., Avruch, I.M., Dutta-Roy, R., Dzierma, Y., Edenhofer, P., Folkner, W.M., Gervits, L.I., Johnston, D.V., Plettmeier, D., Pogrebenko, S.V., Preston, R.A., Tyler, G.L., 2005. The vertical profile of winds on Titan. *Nature* 438, 800–802.
- Bouchez, A.H., 2003. Seasonal trends in Titan's atmosphere: Haze, wind, and clouds. Ph.D. dissertation, California Institute of Technology. URL: <http://resolver.caltech.edu/CaltechETD:etd-10272003-092206>.
- Conrath, B.J., Gierasch, P.J., Ustinov, E.A., 1998. Thermal structure and para hydrogen fraction on the outer planets from Voyager IRIS measurements. *Icarus* 135, 501–517.
- Coustenis, A., Bézard, B., 1995. Titan's atmosphere from Voyager infrared observations. IV. Latitudinal variations of temperature and composition. *Icarus* 115, 126–140.
- Coustenis, A., Achterberg, R.K., Conrath, B.J., Jennings, D.E., Marten, A., Gautier, D., Nixon, C.A., Flasar, F.M., Teanby, N.A., Bézard, B., Samuel-

- son, R.E., Carlson, R.C., Lellouch, E., Bjoraker, G.L., Romani, P.N., Taylor, F.W., Irwin, P.G.J., Fouchet, T., Hubert, A., Orton, G.S., Kunde, V.G., Vinatier, S., Mondellini, J., Abbas, M.M., Courtin, R., 2007. The composition of Titan's stratosphere from Cassini/CIRS mid-infrared spectra. *Icarus* 189, 35–62.
- Fast, K.E., Kostiuk, T., Espenak, F., Buhl, D., Livengood, T.A., Goldstein, J., 1994. Direct measurement of Doppler shifts due to zonal winds on Titan. *Bull. Am. Astron. Soc.* 26, 1183.
- Flasar, F.M., Conrath, B.J., 1990. Titan's stratospheric temperatures: A case for dynamical inertia? *Icarus* 85, 346–354.
- Flasar, F.M., Samuelson, R.E., Conrath, B.J., 1981. Titan's atmosphere: Temperature and dynamics. *Nature* 292, 693–698.
- Flasar, F.M., Kunde, V.G., Abbas, M.M., Achterberg, R.K., Ade, P., Barucci, A., Bézard, B., Bjoraker, G.L., Brasunas, J.C., Calcutt, S., Carlson, R., Cessarsky, C.J., Conrath, B.J., Coradini, A., Courtin, R., Gautier, D., Gierasch, P.J., Grossman, K., Irwin, P., Jennings, D.E., Lellouch, E., Mamoutkine, A.A., Marten, A., Meyer, J.P., Nixon, C.A., Orton, G.S., Owen, T.C., Pearl, J.C., Prange, R., Raulin, F., Read, P.L., Romani, P.N., Samuelson, R.E., Segura, M.E., Showalter, M.R., Simon-Miller, A.A., Smith, M.D., Spencer, J.R., Spilker, L.J., Taylor, F.W., 2004. Exploring the Saturn system in the thermal infrared: The composite infrared spectrometer. *Space Sci. Rev.* 115, 169–297.
- Flasar, F.M., Achterberg, R.K., Conrath, B.J., Gierasch, P.J., Kunde, V.G., Nixon, C.A., Bjoraker, G.L., Jennings, D.E., Romani, P.N., Simon-Miller, A.A., Bézard, B., Coustenis, A., Irwin, P.G.J., Teanby, N.A., Brasunas, J., Pearl, J.C., Segura, M.E., Carlson, R.C., Mamoutkine, A., Schinder, P.J., Barucci, A., Courtin, R., Fouchet, T., Gautier, D., Lellouch, E., Marten, A., Prangè, R., Vinatier, S., Strobel, D.F., Calcutt, S.B., Read, P.L., Taylor, F.W., Bowles, N., Samuelson, R.E., Orton, G.S., Spilker, L.J., Owen, T.C., Spencer, J.R., Showalter, M.R., Ferrari, C., Abbas, M.M., Raulin, F., Edgington, S., Ade, P., Wishnow, E.H., 2005. Titan's atmospheric temperatures, winds, and composition. *Science* 308, 975–978.
- Folkner, W.M., Asmar, S.W., Border, J.S., Franklin, G.W., Finley, S.G., Gorelik, J., Johnston, D.V., Kerzhanovich, V.V., Lowe, S.T., Preston, R.A., Bird, M.K., Dutta-Roy, R., Allison, M., Atkinson, D.H., Edenhofer, P., Plette-meier, D., Tyler, G.L., 2006. Winds on Titan from ground-based tracking of the Huygens probe. *J. Geophys. Res.* 111, doi:10.1029/2005JE002649. E07S02.
- Fulchignoni, M., Ferri, F., Angrilli, F., Ball, A.J., Barn-Nun, A., Barucci, M.A., Bettanini, C., Bianchini, G., Borucki, W., Colombatti, G., Coradini, M., Coustenis, A., Debei, S., Falkner, P., Fanti, G., Flamini, E., Gaborit, V., Gard, R., Hamelin, M., Harri, A.M., Hathi, B., Jernej, I., Leese, M.R., Lehto, A., Lion Stoppato, P.F., López-Moreno, J.J., Mäkinen, T., McDonnell, J.A.M., McKay, C.P., Molina-Cuberos, G., Neubauer, F.M., Pirronello, V., Rodrigo, R., Saggin, B., Schwingenschuh, K., Seiff, A., Simões, F., Svedhem, H., Tokano, T., Towner, M.C., Trautner, R., Withers, P., Zarnecki, J.C., 2005. In situ measurements of the physical characteristics of Titan's environment. *Nature* 438, 785–791.
- Hitchman, M.H., Gille, J.C., Rodgers, C.D., Brasseur, G., 1989. The separated polar winter stratosphere: A gravity wave driven climatological feature. *J. Atmos. Sci.* 46, 410–422.
- Holton, J., 2004. *An Introduction to Dynamic Meteorology*, fourth ed. Elsevier, San Diego.
- Hourdin, F., Talagrand, O., Sadourny, R., Courtin, R., Gautier, D., McKay, C.P., 1995. Numerical simulation of the general circulation of the atmosphere of Titan. *Icarus* 117, 358–374.
- Hourdin, F., Lebonnois, S., Luz, D., Rannou, P., 2004. Titan's stratospheric composition driven by condensation and dynamics. *J. Geophys. Res.* 109, doi:10.1029/2004JE002282. E12005.
- Hubbard, W.B., Sicaudy, B., Miles, R., Hollis, A.J., Forrest, R.W., Nicolson, I.K.M., Appleby, G., Beisker, W., Bittner, C., Bode, H.-J., Bruns, M., Denzau, H., Nezel, M., Riedel, E., Struckmann, H., Arlot, J.E., Roques, F., Sevre, F., Thuillot, W., Hoffmann, M., Geyer, E.H., Buil, C., Colas, F., Lecacheux, J., Klotz, A., Thouvenot, E., Vidal, J.L., Carreira, E., Rossi, F., Blanco, C., Cristaldi, S., Nevo, Y., Reitsema, H.J., Brosch, N., Cernis, K., Zdanavicius, K., Wasserman, L.H., Hunten, D.M., Gautier, D., Lellouch, E., Yelle, R.V., Rizk, B., Flasar, F.M., Porco, C.C., Toubanc, D., Corugedo, G., 1993. The occultation of 28 Sgr by Titan. *Astron. Astrophys.* 269, 541–563.
- Jacquinet-Husson, N., Scott, N.A., Chedin, A., Garceran, K., Armante, R., Chursin, A.A., Barbe, A., Birk, M., Brown, L.R., Camy-Peyret, C., Clerbaux, C., Coheur, P.F., Dana, V., Daumont, L., Debaker-Barilly, M.R., Gaud, J.M., Goldman, A., Hamdouni, A., Hess, M., Jacquenmart, D., Kipke, P., Mandin, J.Y., Massie, S., Mickhailenko, S., Nemchinov, V., Nikitin, A., Newnham, D., Perrin, A., Perevalov, V.I., Regalia-Jarlot, L., Rublev, A., Schreier, F., Schult, I., Smith, K.M., Tashkun, S.A., Teffo, J.L., Toth, R.A., Tyuterev, V.G., Vander Auwera, J., Varanasi, P., Wagner, G., 2005. The 2003 edition of the GEISA/IASI spectroscopic data base. *J. Quant. Spectrosc. Radiat. Trans.* 95, 429–467.
- Kostiuk, T., Livengood, T.A., Hewagama, T., Sonnadend, G., Fast, K.E., Murakawa, K., Tokunaga, A.T., Annen, J., Buhl, D., Schmülling, F., 2005. Titan's stratospheric zonal wind, temperature, and ethane abundance a year prior to Huygens insertion. *Geophys. Res. Lett.* 32, doi:10.1029/2005GL023897. 22205.
- Lacis, A.A., Oinas, V., 1991. A description of the correlated *k* distribution method for modeling nongray gaseous absorption, thermal emission, and multiple scattering in vertically inhomogeneous atmospheres. *J. Geophys. Res.* 96, 9027–9063.
- Lemmon, M.T., Karkoschka, E., Tomasko, M., 1993. Titan's rotation: Surface feature observed. *Icarus* 103, 329–332.
- Lorenz, R.D., Smith, P.H., Lemmon, M.T., Karkoschka, E., Lockwood, G.W., Caldwell, J., 1997. Titan's north-south asymmetry from HST and Voyager imaging: Comparison with models and ground-based photometry. *Icarus* 127, 173–189.
- Niemann, H.B., Atreya, S.K., Bauer, S.J., Carignan, G.R., Demick, J.E., Frost, R.L., Gautier, D., Haberman, J.A., Harpold, D.N., Hunten, D.M., Israel, G., Lunine, J.I., Kasprzak, W.T., Owen, T.C., Paulkovich, M., Raulin, F., Raaen, E., Way, S.H., 2005. The abundances of constituents of Titan's atmosphere from the GCMS instrument on the Huygens probe. *Nature* 438, 779–784.
- Pedlosky, J., 1987. *Geophysical Fluid Dynamics*, second ed. Springer-Verlag, New York, pp. 399–400.
- Press, W.H., Teukolsky, S.A., Vetterling, W.T., Flannery, B.P., 1994. *Numerical Recipes*, second ed. Cambridge Univ. Press, Cambridge, Chapter 18.
- Rannou, P., Hourdin, F., McKay, C.P., Luz, D., 2004. A coupled dynamics-microphysics model of Titan's atmosphere. *Icarus* 170, 443–462.
- Rodgers, C.D., 2000. *Inverse Methods for Atmospheric Sounding*. World Scientific, London.
- Sicaudy, B., Ferri, F., Roques, F., Brosh, N., Nevo, Y., Hubbard, W.B., Reitsema, H.R., Blanco, C., Cristaldi, S., Carreira, E., Rossi, F., Lecacheux, J., Pau, S., Beisker, W., Bittner, C., Bode, H.-J., Bruns, M., Denzau, H., Nezel, M., Riedel, E., Struckmann, H., Appleby, G., Forrest, R.W., Nicolson, I.K.M., Miles, R., Hollis, A.J., 1999. The structure of Titan's stratosphere from the 28 Sgr occultation. *Icarus* 142, 357–390.
- Sicaudy, B., Colas, F., Widemann, T., Bellucci, A., Beisker, W., Kretlow, M., Ferri, F., Lacour, S., Lecacheux, J., Lellouch, E., Pau, S., Renner, S., Roques, F., Fienga, A., Etienne, C., Martinez, C., Glass, I.S., Baba, D., Nagayama, T., Nagata, T., Itting-Enke, S., Bath, K.-L., Bode, H.-J., Bode, F., Lüdemann, H., Lüdemann, J., Neubauer, D., Tegtmeyer, A., Tegtmeyer, C., Thomé, B., Hund, F., deWitt, C., Fraser, B., Jansen, A., Jones, T., Schoenau, P., Turk, C., Meintjes, P., Fiel, D., Frappa, E., Peyrot, A., Teng, J.P., Vignand, M., Hesler, G., Payet, T., Howell, R.R., Kidger, M., Ortiz, J.L., Naranjo, O., Rosenzweig, P., Rapaport, M., 2006. The two Titan stellar occultations of 14 November 2003. *J. Geophys. Res.* 111, doi:10.1029/2005JE002624. E11S91.
- Steck, T., Höpfner, M., von Clarmann, T., Grabowski, U., 2005. Tomographic retrieval of atmospheric parameters from infrared limb emission observations. *Appl. Opt.* 44, 3291–3301.
- Teanby, N.A., Irwin, P.G.J., de Kok, R., Nixon, C.A., Coustenis, A., Bézard, B., Calcutt, S.B., Bowles, N.E., Flasar, F.M., Fletcher, L., Howett, C., Taylor, F.W., 2006. Latitudinal variations of HCN, HC₃N, and C₂N₂ in Titan's stratosphere derived from Cassini CIRS data. *Icarus* 181, 243–255.
- Teanby, N.A., Irwin, P.G.J., de Kok, R., Vinatier, S., Bézard, B., Nixon, C.A., Flasar, F.M., Calcutt, S.B., Bowles, N.E., Fletcher, L., Howett, C., Taylor, F.W., 2007. Vertical profiles of HCN, HC₃N, and C₂N₂ in Titan's atmosphere derived from Cassini/CIRS data. *Icarus* 186, 364–384.

- Tokano, T., Neubauer, F.M., Laube, M., McKay, C.P., 1999. Seasonal variation of Titan's atmospheric structure simulated by a general circulation model. *Planet. Space Sci.* 47, 493–520.
- Vinatier, S., Bézard, B., Fouchet, T., Teanby, N.A., de Kok, R., Irwin, P.G.J., Conrath, B.J., Nixon, C.A., Romani, P.N., Flasar, F.M., Coustenis, A., 2007. Vertical abundance profiles of hydrocarbons in Titan's atmosphere at 15° S and 80° N retrieved from Cassini/CIRS spectra. *Icarus* 188, 120–138.
- Worden, J.R., Bowman, K.W., Jones, D.B., 2004. Two-dimensional characterization of atmospheric profile retrievals from limb sounding observations. *J. Quant. Spectrosc. Radiat. Trans.* 86, 45–71.